Optics Letters

Liquid-crystal-integrated metadevice: towards active multifunctional terahertz wave manipulations

ZHIXIONG SHEN,[1] SHENGHANG ZHOU,[1] SHIJUN GE,[1,2] WEI DUAN,[1] PENG CHEN,[1] LEI WANG,[3] WEI HU,[1,2,*] AND YANQING LU[1]

[1]National Laboratory of Solid State Microstructures, Collaborative Innovation Center of Advanced Microstructures and College of Engineering and Applied Sciences, Nanjing University, Nanjing 210093, China
[2]Institute for Smart Liquid Crystals, JITRI, Changshu 215500, China
[3]College of Electronic and Optical Engineering and College of Microelectronics, Nanjing University of Posts and Telecommunications, Nanjing 210023, China
*Corresponding author: huwei@nju.edu.cn

Received 10 August 2018; revised 2 September 2018; accepted 2 September 2018; posted 4 September 2018 (Doc. ID 342070); published 21 September 2018

Active terahertz elements with multifunction are highly expected in security screening, nondestructive evaluation, and wireless communications. Here, we propose an innovative terahertz metadevice that exhibits distinguishing functions for transmitted and reflected waves. The device is composed of a thin liquid crystal layer sandwiched by Au comb electrodes and a dual-ring resonator array. For transmission mode, the metadevice manifests the electromagnetically induced transparency analog. For reflection mode, it works as a perfect absorber. The comb electrodes actuate the in-plane switching of liquid crystals, making the metadevice actively tuned. 60 GHz frequency tuning of an electromagnetically induced transparency analog and 15% modulation depth of the absorption are demonstrated. Such modulations can be realized in the millisecond scale. The in-plane switching driving mode avoids the electrode connections among separate resonators, thus freeing the design of the metadevice. The proposed work may pave a bright road towards various active multifunctional terahertz apparatuses.

OCIS codes: (300.6495) Spectroscopy, terahertz; (160.3710) Liquid crystals; (160.3918) Metamaterials.

https://doi.org/10.1364/OL.43.004695

The terahertz (THz) wave, typically defined as the frequency range of 0.1–10 THz in the electromagnetic spectrum, holds great potential in security checks, biological detection, and wireless communications [1]. The past few years have witnessed an impressive progress in THz technology. Compared with the well-established THz emitters and detectors, devices capable to efficiently manipulate THz waves are still lacking, especially tunable ones. It is imperative to develop THz filters, switches, lenses, and polarization controllers. Metamaterials are considered as vibrant candidates for THz modulations thanks to their compact size and excellent flexibility in design. Additionally, they reveal exotic electromagnetic properties such as artificial magnetism [2], negative index [3], and chirality [4], most of which are not observed in nature. Unfortunately, the functions of such materials, which are determined by geometries, are usually fixed after fabrication and lack tunability, thus limiting their practical applications. To tackle this challenge, the concept of a metadevice is proposed [5]. Via hybridizing metamaterials with functional matters, including phase-change media [6,7], semiconductors [8,9], graphene [10], and liquid crystals (LCs) [11–13], such devices are endowed with particular dynamic electromagnetic responses.

LCs possess broadband large birefringence with pronounced electrotunability. Through properly applying external field or specifically prealigning the LC, a THz wave can be freely manipulated [14,15]. However, due to the larger wavelength of a THz beam, much thicker cells are required compared to those utilized in a visible or telecom band (usually over 2 orders). As the elastic restoring time is proportional to the square of the LC cell gap, the responses of LC THz devices are very slow (in minute scale). Besides, the large cell gap leads to high operating voltage. They severely restrict applications of these devices. For LC-integrated metadevices, the change of refractive index is taken into account instead of the phase retardation. Therefore, the cell gap along with corresponding issues could be drastically decreased. Recently, various LC THz metadevices have been proposed, and their utilizations as perfect absorbers [16], polarization converters [17], and phase shifters [18] have been demonstrated. Until now, such devices still encounter some challenges. First, most LC-integrated metadevices are biased vertically, and electric connections are required on both superstrate and substrate. The connections may severely influence the resonant properties, thus restricting their functions. Second, the device works in either transmission or reflection mode and only a single function is realized. To further exploit active multifunctional LC-integrated metadevices for THz wave manipulation is a meaningful and urgent task.

In this Letter, we introduce a subwavelength comb electrode onto the substrate as both a polarization beam splitter and an in-plane switching (IPS) electrode [13], and a dual-ring resonator array onto the superstrate as the metasurface for THz wave manipulation. LC is infiltrated as the intermedium with a tunable refractive index. On the basis of this design, a THz metadevice that works as an electromagnetically induced transparency (EIT) analog in transmission mode and a THz absorber in reflection mode are proposed. As the LC is in-plane switched, connections among separate resonators on the superstrate are avoided, freeing the design of such a metadevice. Active tuning as fast as millisecond scale is realized via electrically driving. The proposed design could be extended to various active multifunctional THz metadevices.

The configuration of the device is illustrated in Fig. 1. Both the substrate and superstrate are 500-μm-thick fused silica and separated by a 5-μm-diameter spacer. A homemade high-birefringence LC NJU-LDn-4 with an average birefringence of 0.3 from 0.5 to 2.5 THz is infiltrated [19]. The superstrate is covered with the Au dual-ring resonator array. As shown in Fig. 1(c), each unit contains an outside closed ring resonator (CRR) and an inside split-ring resonator (SRR), which are aligned eccentrically. The substrate is covered with Au subwavelength comb electrodes, as revealed in Fig. 1(d). The subwavelength grating is 10 μm in pitch with a duty cycle of 50%. It transmits a transverse magnetic wave (TM wave, the electric field vector of the incident wave is parallel to the grating vector), while it reflects the transverse electric wave (TE wave, the electric field vector is perpendicular to the grating vector), as shown in the inset of Fig. 1(d). Both substrates are spin-coated with a sulfonic azo dye (SD1, Dainippon Ink and Chemicals Inc., Chiba, Japan) alignment layer [20] to guide the LC orientation to be perpendicular to the grating vector.

The metasurface and comb electrodes are fabricated using the standard photolithography technique. After that, electron beam evaporation is applied to deposit 200 nm Au. Samples are soaked in acetone to lift off the undesired Au. The metasurface and comb electrodes are spin-coated at 3000 rpm for 30 s with the SD1 solution dissolved in N, N-dimethylformamide (DMF). Then, the substrates are baked at 100°C for 10 min to remove the DMF. After that, an exposure of 3 J/cm^2 under a linearly polarized 405 nm blue LED is applied to introduce homogeneous alignment. Finally, the two substrates are assembled to form a cell, and the LC is infiltrated.

The principle of the device is distinguishing for transmitted and reflected waves. In transmission mode, only polarization parallel to the grating vector, defined as E_x, is transmitted. In this case, the inside SRR supports the inductive capacitive (LC) resonance and interacts weakly with E_x. It causes a transmission spectrum with a sharp linewidth, while the outside CRR supports a strong dipolar resonance featured by a transmission spectrum with a broad linewidth. Through optimizing the structural parameters, we make both resonances occur at the same frequency. Their near fields interfere with each other and form an EIT analog [21]. In Fig. 2(a), a transmission peak appears at 1.30 THz. The electric field and current density of a single unit at 1.30 THz are presented in Figs. 2(b) and 2(c), respectively. As exhibited in Fig. 2(b), the top view image indicates that the near fields of SRR and CRR are strongly coupled, while the side view image reveals that little interference occurs between the metasurface and the Au grating. In Fig. 2(c), the induced surface currents in inside SRR and outside CRR run in opposite directions, causing destructive interference. Therefore, a sharp transmission peak appears. In reflection mode, only polarization perpendicular to the grating vector, defined as E_y, is reflected. In this case, the grating totally reflects the TE wave like a mirror, and the whole metadevice is analogous to a metamaterial absorber (MMA) [11,22].

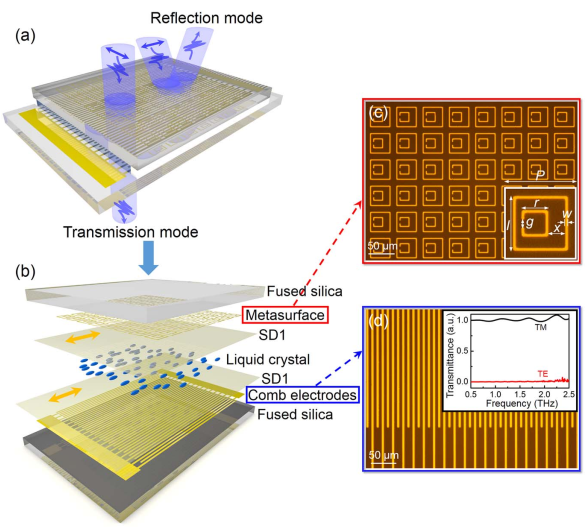

Fig. 1. (a) Schematic illustration and (b) decomposition diagram of the designed metadevice. The yellow arrows indicate the alignment direction. The micrographs of (c) the metasurface and (d) the comb electrode. Inset in (c) shows the unit dimension of the resonator; p, lattice periodicity: 50 μm; l, CRR length: 40 μm; r, SRR length: 20 μm; w, structure width: 3 μm; g, gap: 4 μm; and x, asymmetry distance: 11 μm. The inset in (d) shows the polarization selectivity of the subwavelength grating.

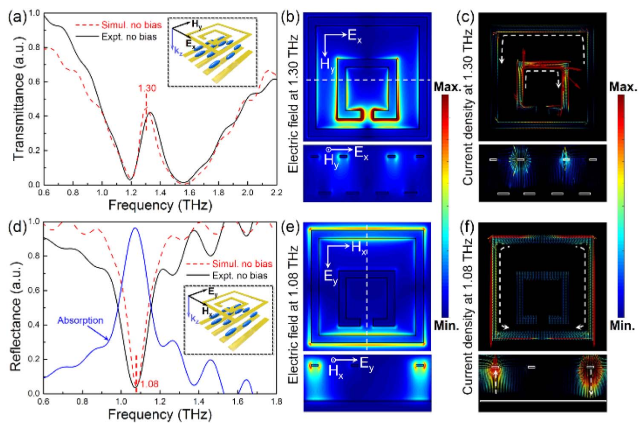

Fig. 2. (a) Numerical simulation and measured spectra of the metadevice in transmission mode. The (b) electric field and (c) current density of a single unit at 1.30 THz. (d) Numerical simulation and measured spectra of the metadevice in reflection mode. The blue line depicts the calculated absorption spectrum. The (e) electric field and (f) current density of a single unit at 1.08 THz. The incident polarizations are labeled in insets of (a) and (d). The white dashed arrows in (c) and (f) depict the directions of the induced surface currents.

Figure 2(d) reveals the reflection spectrum with an absorption peak (97%) at 1.08 THz (A = 1-R-T). The top view image in Fig. 2(e) shows that the electric field is primarily localized on up and down sides of the CRR. The top view image in Fig. 2(f) indicates that the surface currents are parallel to E_y. The above facts suggest an electric dipole resonance. The side view images in Figs. 2(e) and 2(f) reveal antiparallel currents between the metasurface and the grating, resulting in a magnetic dipole resonance. Therefore, the metadevice couples to both electric and magnetic fields of the incident wave and is able to completely dissipate the incident energy at the resonant frequency. All the numerical simulations are carried out using Lumerical FDTD Solutions. Metasurface and comb electrodes are set as conductive materials with DC conductivity, $\sigma_{\mathrm{DC}} = 4.09 \times 10^7$ S/m. The refractive index of silica is set as 1.92. In our simulation, the dielectric anisotropy of the LC layer is fully taken into account.

The metadevice can be actively tuned thanks to the electro-optical tunability of LC. The refractive index of NJU-LDn-4 can be switched between n_o $(1.5 + i0.05)$ and n_e $(1.8 + i0.03)$ by the electric field. Here, the feature size of the metamaterial is in the micrometer scale and has little influence on LC anchoring. Thus, it will not limit the tunability of LC-integrated metadevices compared to those in visible and near-infrared range [23]. Schematics of LC orientations at bias OFF and ON states are illustrated in Figs. 3(a) and 3(b). The LC is homogeneously prealigned in a direction perpendicular to the grating vector [Fig. 3(a)]. After bias is applied, the IPS electrodes generate the comb electric field. The electric field vectors above the electrodes point mainly along the z axis, and the electric field vectors between the electrodes point mainly along the x axis. The LC orientation follows this fringe electric field [Fig. 3(b)]. Simulations of LC orientations at different voltages are carried out using a 3D module of the commercial software Techwiz LCD and are presented in Figs. 3(c)–3(f). As expected, the LC orientation is along the y axis at 0 V. Along with the voltage rising up, LCs adjacent to the electrodes start to reorient whereas LCs near the superstrate remain in the original direction due to the weak electric field there. Finally, LCs above the electrodes stand up along the z axis whereas LCs between electrodes reorient along the x axis. Over 45 V (saturating voltage), further increasing the voltage will not change the LC orientations. It needs to be noticed that the LC orientation is not uniformly tuned, thus limiting the modulation depth of the device compared to that of the vertical bias mode.

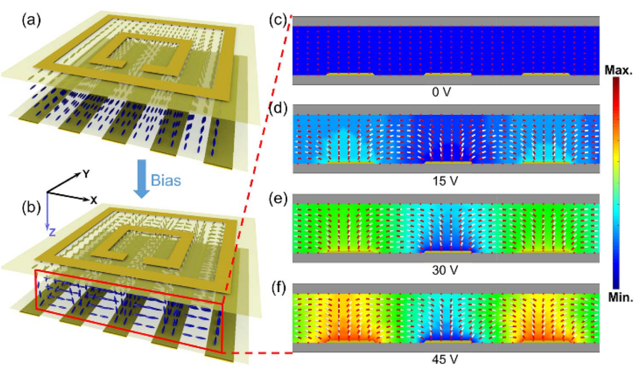

Fig. 3. (a) and (b) Schematic illustrations of LC orientations at bias OFF and ON states. (c)–(f) The simulated LC orientations with different applied voltages: (c) 0 V, (d) 15 V, (e) 30 V, and (f) 45 V. The color bar represents the local electric field intensity. The red and white rods depict the local LC orientations.

A THz time-domain spectroscopy (THz-TDS) (TAS7400SP; Advantest Corporation, Tokyo, Japan) is used to characterize the performance of such an active dual-mode metadevice. Corresponding setup for transmission mode is exhibited in Fig. 4(a). We use an empty cell with two 500-μm-thick silica substrates separated by a 5 μm spacer as reference. The metadevice is driven by a 1 kHz square-wave alternating voltage signal. The voltage-dependent transmittance is illustrated in Fig. 4(b). The transmission peak of the EIT analog redshifts from 1.33 THz to 1.27 THz, and the modulation depth of 37% is obtained at 1.27 THz $[(T_{45V} - T_{0V})/T_{45V}]$. Corresponding numerical simulations verify the same frequency redshift along with the voltage increasing. At the transmission peak, the surface currents in SRR and CRR run antiparallelly and predominantly accumulate along the x axis [Fig. 2(c)]. Thus, the resonant frequency is particularly sensitive to the refractive index change along the same direction. In our experiment, the refractive index of LC between the electrodes changes from n_o to n_e with bias. Therefore, a significant shift of the resonance is realized. The active tuning of the EIT effect has potential in the research of slow light behaviors and strong-dispersion THz devices [24].

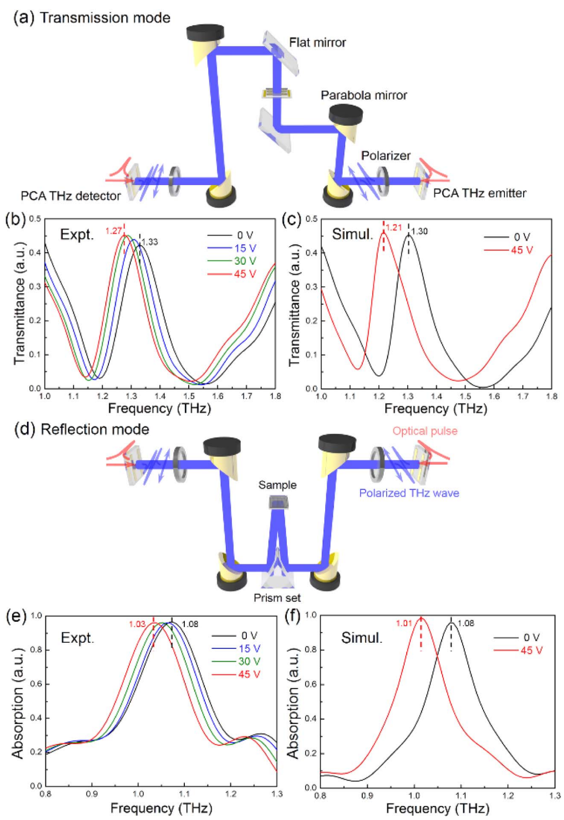

Fig. 4. (a) Transmission mode setup of the THz-TDS. (b) Measured transmission spectra of the metadevice at 0 V, 15 V, 30 V, and 45 V. (c) Corresponding simulation results at 0 V and 45 V. (d) The reflection mode setup of the THz-TDS. (e) Measured absorption spectra of the metadevice at 0 V, 15 V, 30 V, and 45 V. (f) Corresponding simulation results at 0 V and 45 V.

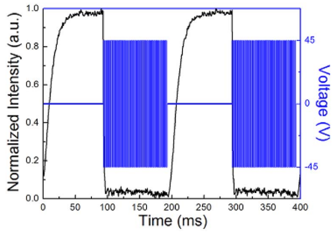

Fig. 5. Black line reveals the electro-optical response of the device at 45 V. The blue line depicts the 1 kHz square-wave voltage signals.

The setup for reflection mode measurement is revealed in Fig. 4(d). A single 500-μm-thick silica with Au film covered on the back side is utilized as the reference. The absorption peaks reach 97% and redshift by 50 GHz when the bias changes from 0 V to 45 V [Fig. 4(e)]. A modulation depth of 15% is reached at 1.03 THz for the absorption $[(A_{45\mathrm{V}} - A_{0\mathrm{V}})/A_{45\mathrm{V}}]$. Corresponding numerical simulations [Fig. 4(f)] are consistent with the above results. As mentioned above, such an absorber works on the resonance between the metasurface and comb electrodes. The electric field vector points mainly along the z axis in the LC layer. Thus, the resonance is affected by the refractive index change of LC along the z axis [25]. When bias is applied, LCs above the electrodes are reoriented vertically, so the refractive index changes from n_o to n_e in the z axis, resulting in the resonance redshift. The tunable absorber can be widely utilized in active sensors, energy harvesting, and spatial light modulators [12,26]. It needs to be noticed that the simulated tuning ranges in both transmission and reflection modes (90 GHz and 70 GHz, respectively) are slightly larger than the measurements. This is mainly due to the insufficient LC actuation caused by the imperfect fabrication of electrodes. To extend the tuning range, more precise fabrication and larger birefringence LCs could be adopted.

Both the cell gap and the distance between adjacent electrodes are 5 μm, permitting the fast response of the proposed metadevice. As the response is independent of the working wavelength, the measurement is carried out using a 633 nm laser beam transmitting the device. In the characterization, a 1 kHz square-wave voltage signal is applied with the bias alternating between the ON and OFF state, lasting for 100 ms each. When the bias is OFF, the transmission amplitude of the beam is centered at zeroth order. When the bias is ON, the periodic LC orientation distribution is induced by the IPS biasing mode, leading to a diffraction. Thus, the transmission amplitude is dramatically decreased at zeroth order. We measure the photovoltage of the zeroth order and normalize it to intensity. Its switching property on 45 V is illustrated in Fig. 5. The response time is 2.4 ms for bias OFF to ON, while 26 ms for the reverse process. The performance could be further improved via properly selecting LCs and optimizing the electrode geometry.

In summary, we introduce, to the best of our knowledge, a novel LC-integrated THz metadevice. It plays the role of an EIT analog in transmission mode and works as a perfect absorber in reflection mode. Through reorienting the LCs with voltages applied on IPS electrodes, fast and active tuning of both functions are realized. The proposed design enables free tailoring of metasurfaces, permitting versatile manipulations of THz waves. This work supplies a practical way for fabricating active multifunctional THz metadevices, and may inspire various advanced THz apparatuses.

Funding. National Natural Science Foundation of China (NSFC) (61435008, 61575093); Ministry of Science and Technology of the People's Republic of China (MOST) (2017YFA0303700); Natural Science Foundation of Jiangsu Province (BK20150845, SBK2018010313).

REFERENCES

1. B. Ferguson and X. C. Zhang, Nat. Mater. **1**, 26 (2002).
2. T. J. Yen, W. J. Padilla, N. Fang, D. C. Vier, D. R. Smith, J. B. Pendry, D. N. Basov, and X. Zhang, Science **303**, 1494 (2004).
3. S. Zhang, Y. S. Park, J. Li, X. Lu, W. Zhang, and X. Zhang, Phys. Rev. Lett. **102**, 023901 (2009).
4. S. Zhang, J. Zhou, Y. S. Park, J. Rho, R. Singh, S. Nam, A. K. Azad, H. T. Chen, X. Yin, A. J. Taylor, and X. Zhang, Nat. Commun. **3**, 942 (2012).
5. N. I. Zheludev and Y. S. Kivshar, Nat. Mater. **11**, 917 (2012).
6. T. Driscoll, H. T. Kim, B. G. Chae, B. J. Kim, Y. W. Lee, N. M. Jokerst, S. Palit, D. R. Smith, M. Di Ventra, and D. N. Basov, Science **325**, 1518 (2009).
7. M. Seo, J. Kyoung, H. Park, S. Koo, H. S. Kim, H. Bernien, B. J. Kim, J. H. Choe, Y. H. Ahn, H. T. Kim, N. Park, Q. H. Park, K. Ahn, and D. S. Kim, Nano Lett. **10**, 2064 (2010).
8. H. T. Chen, W. J. Padilla, J. M. O. Zide, A. C. Gossard, A. J. Taylor, and R. D. Averitt, Nature **444**, 597 (2006).
9. J. Gu, R. Singh, X. Liu, X. Zhang, Y. Ma, S. Zhang, S. A. Maier, Z. Tian, A. K. Azad, H. T. Chen, A. J. Taylor, J. Han, and W. Zhang, Nat. Commun. **3**, 1151 (2012).
10. L. Ju, B. Geng, J. Horng, C. Girit, M. Martin, Z. Hao, H. A. Bechtel, X. Liang, A. Zettl, Y. R. Shen, and F. Wang, Nat. Nanotechnol. **6**, 630 (2011).
11. D. Shrekenhamer, W. C. Chen, and W. J. Padilla, Phys. Rev. Lett. **110**, 177403 (2013).
12. S. Savo, D. Shrekenhamer, and W. J. Padilla, Adv. Opt. Mater. **2**, 275 (2014).
13. C. C. Chen, W. F. Chiang, M. C. Tsai, S. A. Jiang, T. H. Chang, S. H. Wang, and C. Y. Huang, Opt. Lett. **40**, 2021 (2015).
14. L. Wang, X. W. Lin, W. Hu, G. H. Shao, P. Chen, L. J. Liang, B. B. Jin, P. H. Wu, H. Qian, Y. N. Lu, X. Liang, Z. G. Zheng, and Y. Q. Lu, Light Sci. Appl. **4**, e253 (2015).
15. S. J. Ge, P. Chen, Z. X. Shen, W. F. Sun, X. K. Wang, W. Hu, Y. Zhang, and Y. Q. Lu, Opt. Express **25**, 12349 (2017).
16. L. Wang, S. Ge, W. Hu, M. Nakajima, and Y. Lu, Opt. Express **25**, 23873 (2017).
17. B. Vasić, D. C. Zografopoulos, G. Isić, R. Beccherelli, and R. Gajić, Nanotechnology **28**, 124002 (2017).
18. Y. Y. Ji, F. Fan, M. Chen, L. Yang, and S. J. Chang, Opt. Express **25**, 11405 (2017).
19. L. Wang, X. W. Lin, X. Liang, J. B. Wu, W. Hu, Z. G. Zheng, B. B. Jin, Y. Q. Qin, and Y. Q. Lu, Opt. Mater. Express **2**, 1314 (2012).
20. P. Chen, L. L. Ma, W. Duan, J. Chen, S. J. Ge, Z. H. Zhu, M. J. Tang, R. Xu, W. Gao, T. Li, W. Hu, and Y. Q. Lu, Adv. Mater. **30**, 1705865 (2018).
21. M. Manjappa, S. Y. Chiam, L. Q. Cong, A. A. Bettiol, W. L. Zhang, and R. Singh, Appl. Phys. Lett. **106**, 181101 (2015).
22. N. I. Landy, S. Sajuyigbe, J. J. Mock, D. R. Smith, and W. J. Padilla, Phys. Rev. Lett. **100**, 207402 (2008).
23. O. Buchnev, N. Podoliak, M. Kaczmarek, N. I. Zheludev, and V. A. Fedotov, Adv. Opt. Mater. **3**, 674 (2015).
24. P. Prakash, M. Manukumara, H. C. Pei, S. Ranjan, S. Navab, and L. Chengkuo, Adv. Opt. Mater. **4**, 541 (2016).
25. G. Isić, B. Vasić, D. C. Zografopoulos, R. Beccherelli, and R. Gajić, Phys. Rev. Appl. **3**, 064007 (2015).
26. L. Q. Cong, S. Y. Tan, R. Yahiaoui, F. P. Yan, W. L. Zhang, and R. Singh, Appl. Phys. Lett. **106**, 031107 (2015).